48.0 GRAIN BOUNDARY FRACTURE ANALYSIS IN ALUMINUM

Scott Blazanin (ISU)
Faculty: Pete Collins (ISU)
Industrial Mentor: Matt Krug (AFRL)

This project was initiated in November 2020 and is being supported by the Air Force Research Laboratory (AFRL) with industrial mentorship provided by Matt Krug. The research performed during this project will serve as a basis for the M.S. thesis project for Scott Blazanin.

48.1 Project Overview and Industrial Relevance

The demand for lighter, faster, and stronger aircraft has begun to push existing material-geometry combinations to their design limits. Over 95% of structural aircraft parts are made from aluminum and titanium alloys and polymer matrix composites [48.1]. Of these, aluminum alloys have often been a dominant choice owing to their good corrosion resistance, high specific strength, damage tolerance, and matured processing and inspection technologies [48.2]. In addition to material improvements, design changes have been made to enable the manufacture of single component structural supports. This unitized part geometry shows improved performance and reduced weight compared to multi-component parts but must be manufactured from a single thick sheet of material [48.3].

To meet market demand for an improved aluminum alloy with good thick section properties in airframe components, Alcoa developed AA7085 (Al 7085), as a wrought alloy typically composed of (wt%) 7-8 Zn, 1.2-1.8 Mg, 1.3-2 Cu, 0.08-0.15 Zr, 0.08 Fe, 0.06 Si, and balanced with Al [48.4]. This alloy, offered as an upgrade to AA7075, is now being used in primary structural components in the Airbus A380 and Joint Strike Fighter aircrafts [48.2]. When compared to other alloys of the 7xxx series, AA7085 has superior thick section mechanical properties, quench insensitivity, fracture toughness, and fatigue properties while maintaining high specific strength and corrosion resistance [48.4]. Despite advantages over previous generations of aluminum alloys, Al 7085 has shown atypical crack growth behavior under cyclic loading [48.5], which has raised concerns over its viability as a material for structural components in aircrafts. Prior investigations have shown that forged components with certain grain orientations exhibit fatigue cracking behavior resulting in grain boundary delamination and unpredictable crack branching [48.5].

An understanding of the crack branching and grain boundary delamination behavior observed in cyclically loaded Al 7085 may allow for wider application of this material within the aerospace industry. With further characterization and analysis of the fatigue crack growth behavior, improvements can be made to lifecycle predictions and component maintenance for this material.

48.2 Previous Work

48.2.1 Literature Review

Previous research, performed by Neely, studied the fatigue crack growth behavior in Al 7085 plates with different grain orientations, showing that critical stress intensities for crack deviation could be determined using standard testing practices [48.5]. Fatigue testing determined that drops in the stress intensity during fatigue crack propagation correlated with crack deviation from the primary crack direction. Additionally, the severity of crack branching was suggested to be a function of the applied load ratio, with higher load ratios showing more crack bifurcation events [48.5]. It should be noted that the scope of Neely's work does not include a discussion of subsurface crack propagation and that any subsurface damage was only discovered after testing to failure. Macroscopic crack branching events were observed on plate surfaces after cracks had progressed through the thickness of the specimens during testing. Some surface crack deviation events were photographed synchronously with fatigue testing, allowing for stress intensity factors to be paired with pictures of surface crack observations.

Microstructural effects on crack deflection and delamination fractures in varying compositions of aluminum alloys have been widely studied. Rao and Ritchie investigated the effects of microstructure on the mechanical properties and fatigue crack propagation in second generation Al-Li alloys [48.6] and determined that grain anisotropy is a

critical factor in determining fracture toughness. As shown in **Figures 48.1** and **48.2**, the primary crack can interact with the anisotropic grain structure in three different ways [48.6]. Firstly, in longitudinal transverse (L-T or T-L) loading, crack growth occurs transversely across grains. Secondly, in transverse short (T-S or L-S) loading, the crack is arrested by grain boundaries aligned perpendicular to the direction of primary crack growth. Lastly, for short longitudinal (S-T or S-L) loading, crack growth progresses through elongated grain boundaries leading to delamination cracking. The fracture toughness of specimens in delamination cracking orientations (S-L or S-T) was determined to exhibit half the fracture toughness of L-T and T-L orientations, and almost a quarter of the fracture toughness of the T-S orientation [48.6].

Grain boundary characteristics are shown to have a strong effect on crack behavior in laminated aluminum alloys. In Al-Li alloy 2090 forged plate samples, Tayon et al. found that delamination cracking depends on grain boundary characteristics, with brass textured grains of high misorientation presenting increased delamination cracking events [48.8]. Electron backscatter diffraction (EBSD) analysis of neighboring grains that underwent delamination fracture indicated that a large Taylor factor difference in brass-textured grain pairs reliably showed delamination cracking. Large plastic deformation was observed to occur in grains along one edge of a delamination boundary, with local deformation accumulating in grains with low Taylor factors [48.8]. This study supports the hypothesis that high energy grain boundaries and lack of accommodation for local slip correlate with increased delamination cracking events in aluminum alloys.

48.2.2 Sample Preparation and Preliminary Imaging

The samples analyzed in this work are the same plates that Neely used in his study of stress intensity factors and crack deviation in Al 7085 [48.5]. All specimens had middle-cracked fatigue test geometries and were extracted from hand forged plate. For each middle-cracked, hand forged specimen, stress ratios (R) of 0.1, 0.9, and -0.7 were selected. An overview of the sample set is provided in **Table 48.1**. Macroscale images of the as-tested plates can be seen in **Figure 48.3(a-f)**.

The received sample set was imaged using stereomicroscopy for the purposes of creating fracture edge image mosaics and obtaining higher magnification photo-documentation of plate specimens in the as-tested condition. As shown in **Figure 48.4**, the full fracture edge was imaged at a resolution sufficient to identify secondary cracks emerging from the plate surface. For each plate specimen, a minimum of 65 stereomicrographs were taken along each fracture edge and include the full length of primary cracking and approximately 3 centimeters of surrounding plate material along each edge.

All six plate specimens were sent off-site for electrical discharge machine (EDM) sectioning. For each plate, four fracture edge specimens were excised for crack analysis, as well as one section far from the fracture edge for analysis of the base microstructure, as indicated in **Figure 48.5** for specimen MH-TS-07. Following EDM sectioning, through-thickness sectioning was performed just outside the centerline thickness via precision low-speed saw. This thickness was selected to allow for metallographic preparation approaching the centerline where crack network density is highest, as shown in **Figure 48.6**.

In collaboration with scientists at the Air Force Research Laboratory, a procedure was developed for the metallographic preparation of Al 7085 for electron backscatter diffraction (EBSD). The procedure, summarized in **Table 48.2**, was optimized for edge retention and surface cleanliness, both of which are required for accurate indexing of fracture edge grain orientation when obtaining EBSD data. To minimize induced surface deformation and avoid crack widening and poor edge retention, a precision polishing system was used for the preparation of all specimens. The use of a precision polishing system also allowed a way to measure material removal via micrometers installed on the equipment.

48.3 Recent Progress

48.3.1 Secondary Crack Density Analysis

Following metallographic preparation, sample fracture edges were imaged with optical microscopy and fracture edge mosaics compiled, as shown in **Figure 48.7** for MH-LS-01. The optical image mosaics were used to quantify the secondary crack length and density as a function of distance along the primary crack using MIPAR Image Analysis software. During image analysis, information about the total number of secondary cracks, secondary crack length, and the location of each secondary crack along the primary crack edge were extracted. Then, secondary crack lengths and densities were plotted against primary crack length.

To calculate secondary crack density, the total secondary crack length over a sample size of five secondary cracks was divided by the overall horizontal length spanned by the secondary cracks sampled. The location along the primary crack for each sampled group was selected to be the location of the median secondary crack. As shown in **Figures 48.8** and **48.9** for sample MH-LS-01, the length of secondary cracks and the secondary crack density increase with primary crack length.

48.3.2 EBSD Analysis

EBSD maps were collected for each specimen. Regions of interest for EBSD mapping focused on three locations: secondary crack initiation sites, crack regions where the direction of secondary crack propagation relative to the loading axis changed from parallel to perpendicular (or vice-versa), and secondary crack terminations. These regions were selected to investigate the microstructural conditions under which secondary cracks nucleate, grow, change direction, and terminate. Additionally, for each orientation (L-S and T-S), large area EBSD maps were collected for material texture analysis. Pole figures resulting from these large area maps are shown in **Figure 48.10** and show the strong texturing present in both L-S and T-S orientations.

To efficiently analyze EBSD data for all specimen sets, a script was developed using the MATLAB MTEX Toolbox. The script takes a raw EBSD data file and automates the generation of plots and data, some of which include plots of the inverse pole figure in the z-direction (IPF-Z), grain segmentation from which grain misorientations can be assessed, Kernel average misorientation (KAM), and Schmidt factors for individual grains.

Secondary cracks were found to initiate at high angle grain boundaries which, for this work, are being defined as grain boundaries with a misorientation angle higher than 15°. The initiation behavior of secondary cracks, shown in **Figure 48.11**, may suggest that the stress state at the primary crack tip is only sufficient for the initiation of secondary cracks at high-angle grain boundaries. Following nucleation and initial growth along a high angle grain boundary, secondary crack growth is observed to switch from *intergranular* fracture to *intragranular* fracture at a grain boundary triple point at the end of the high angle grain boundary. At this triple point, the grain boundary energy is no longer favorable for intergranular fracture, so the crack progresses through the grain with the highest Schmidt factor. Provided that the secondary crack has sufficient energy to propagate intragranularly, it will continue to propagate through the material, with the crack path preferring the elongated high-angle grain boundaries. An IPF-Z map of a multi-directional segment of a secondary crack on sample MH-LS-01 21A is shown in **Figure 48.12**. At the point where the secondary crack no longer has sufficient energy for intergranular nucleation, the crack growth will terminate. The termination behavior of secondary cracks consistently occurs at the end of high-angle grain boundaries in all loading conditions and orientations studied. An EBSD map for a secondary crack termination region in specimen MH-LS-01 21A is shown in **Figure 48.13**, demonstrating termination along a high-angle grain boundary.

Additionally, analysis of Kernel average misorientation (KAM) was conducted for the selected regions of interest. The local misorientation along secondary crack edges varies with the type of cracking present; either intragranular or intergranular. **Figure 48.14** shows a KAM map of a region of interest where the secondary crack switches direction and type (from intragranular to intergranular). For intergranular cracks progressing along high-angle grain boundaries, low local misorientation is seen. For intragranular crack segments, there is a local increase in the KAM along mating fracture edges. The secondary crack introduces a large amount of strain energy to grains which are

fractured intragranularly; this stored strain energy is clearly seen in KAM maps. For crack segments which follow high-angle grain boundaries, far less strain energy is transferred locally to the mating fracture edge grains, suggesting that high-angle grain boundary fracture progresses in a brittle manner.

48.4 Plans for Next Reporting Period

- Pair secondary crack length and density measurements to macro-scale fatigue crack growth data collected by Neely.
- Finish thesis document describing in full the work completed for this project.
- Defend thesis on May 9th, 2022.
- Prepare a draft to publish the findings of this study.

48.5 References

[48.1] I.J. Polmear, Recent Developments in Light Alloys, Materials Transactions, JIM. 37 (1996) 12–31. doi:10.2320/matertrans1989.37.12.

[48.2] T.R. Prabhu, An Overview of High-Performance Aircraft Structural Al Alloy-AA7085, Acta Metallurgica Sinica (English Letters). 28 (2015) 909–921. doi:10.1007/s40195-015-0275-z.

[48.3] J.T. Burns, J. Boselli, Effect of plate thickness on the environmental fatigue crack growth behavior of AA7085-T7451, International Journal of Fatigue. 83 (2015) 253–268. doi:10.1016/j.ijfatigue.2015.10.020.

[48.4] L. Mueller, L. Suffredini, D. Bush, ALCOA 7085 Forgings: 7th Generation Structural Solutions, 1130cc.Com. (2006). https://www.1130cc.com/forums/attachment.php?attachmentid=485073&d=1471292095 (accessed March 19, 2021).

[48.5] J.A. Neely, Correlation of stress intensity range with deviation of the crack front from the primary crack plane in both hand and die forged aluminum 7085-T7452., thesis, 2019.

[48.6] K.T. Venkateswara Rao, R.O. Ritchie, Mechanical properties of Al–Li alloys Part 1 Fracture toughness and microstructure, Materials Science and Technology. 5 (1989) 882–895. doi:10.1179/mst.1989.5.9.882.

[48.7] K.T. Venkateswara Rao, R.O. Ritchie, Mechanical properties of Al–Li alloys Part 2 Fatigue crack propagation, Materials Science and Technology. 5 (1989) 896–907. doi:10.1179/mst.1989.5.9.896.

[48.8] W. Tayon, R. Crooks, M. Domack, J. Wagner, A.A. Elmustafa, EBSD study of delamination fracture in Al–Li alloy 2090, Experimental Mechanics. 50 (2008) 135–143. doi:10.1007/s11340-008-9202-9.

[48.9] E399-20a Standard Test Method for Linear-Elastic Plane-Strain Fracture Toughness of Metallic Materials, ASTM Compass. (2021). https://doi.org/10.1520/E0399-20A (accessed March 19, 2021).

48.6 Figures and Tables

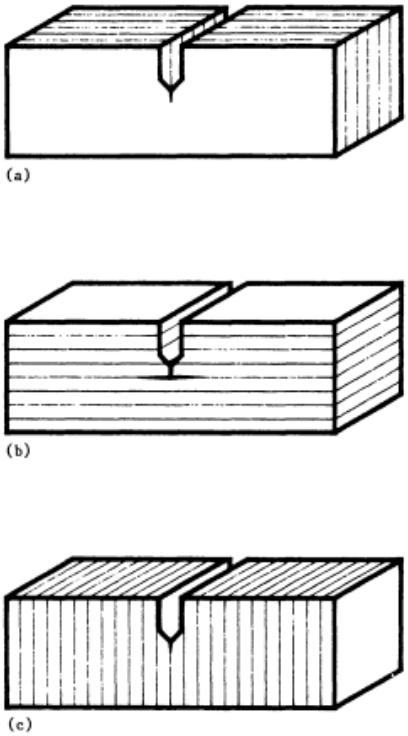

Figure 48.1: Schematic of orientations for crack extension in anisotropic material containing specific planes in one direction; (a) crack dividing orientation corresponding to L-T and T-L, (b) crack arresting orientation corresponding to T-S and L-S, (c) crack delamination orientation corresponding to S-L and S-T [48.6].

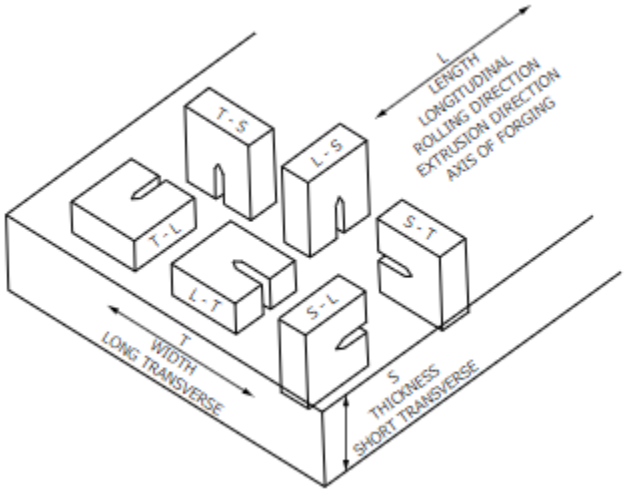

Figure 48.2: Schematic showing different orientations of test specimens that can be excised from a plate [48.9]. For each specimen orientation, the first letter represents the test loading direction while the second letter describes the direction of primary crack growth with respect to the plate. For example, S-L corresponds to a specimen pulled along the thickness of the plate with a primary crack propagating in the longitudinal direction of the plate.

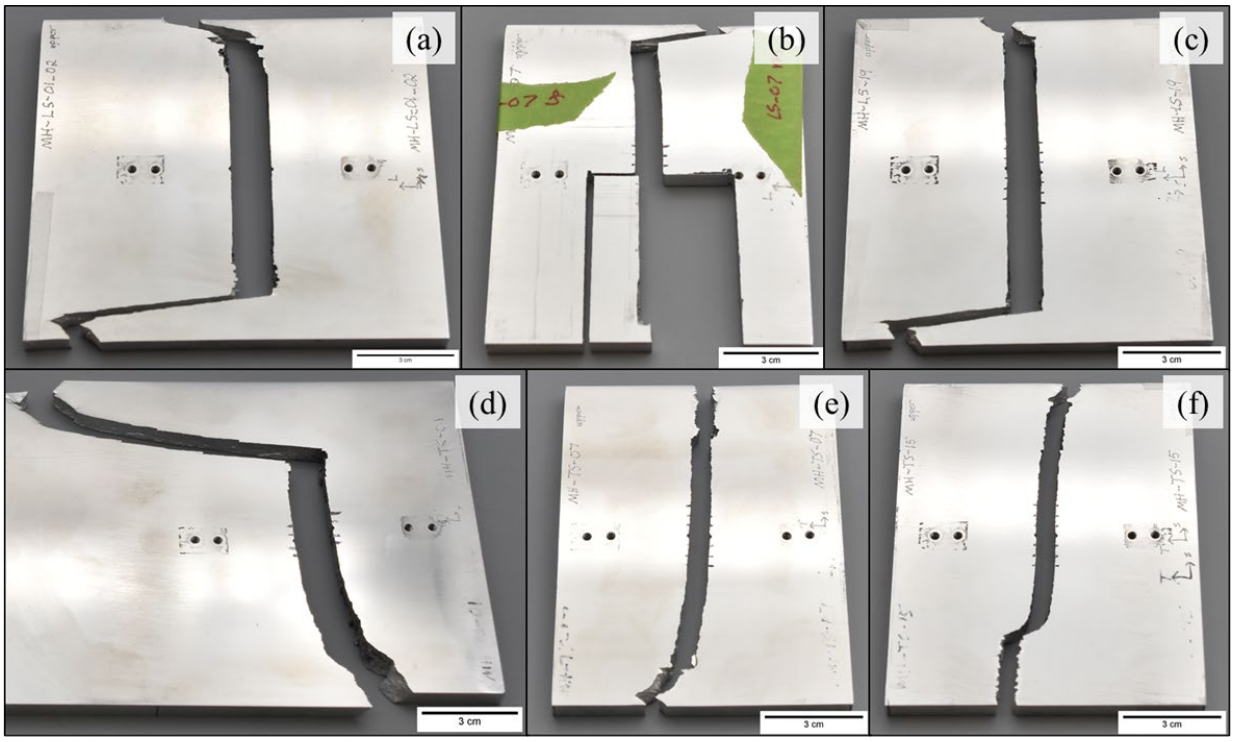

Figure 48.3: Macroscale images of as-tested Al 7085 plate specimens. (a) Specimen MH-LS-01_02, (b) MH-LS-07, (c) MH-LS-19, (d) MH-TS-01, (e) MH-TS-07, (f) MH-TS-19.

Table 48.1: Sample set received from AFRL. The table provides a description of specimen identity, history, and testing conditions. Companion macroscale images are referred to in **Figure 48.3**.

Specimen Name	Grain Orientation	Load Ratio	Image
MH-LS-01_02	L-S	0.1	Figure 48.3a
MH-LS-07	L-S	0.7	Figure 48.3b
MH-LS-19	L-S	-0.9	Figure 48.3c
MH-TS-01	T-S	0.1	Figure 48.3d
MH-TS-07	T-S	0.7	Figure 48.3e
MH-TS-19	T-S	-0.9	Figure 48.3f

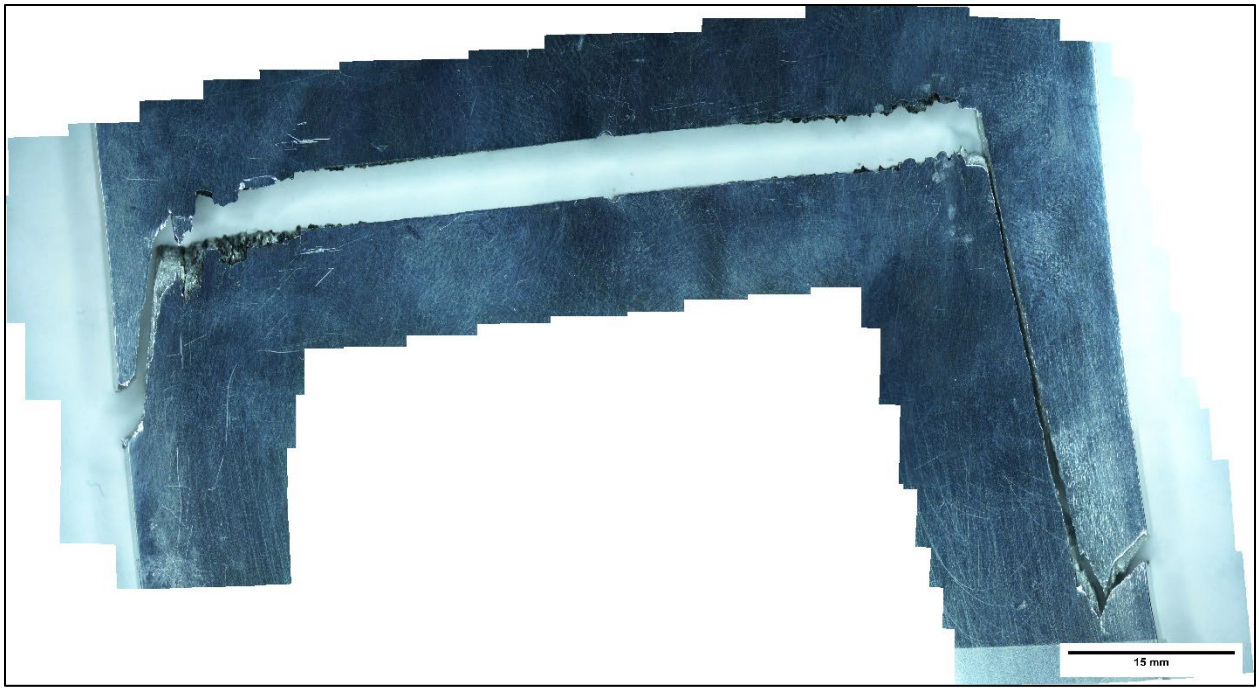

Figure 48.4: Image mosaic from stereomicrographs along the full fracture edge of plate MH-LS-01.

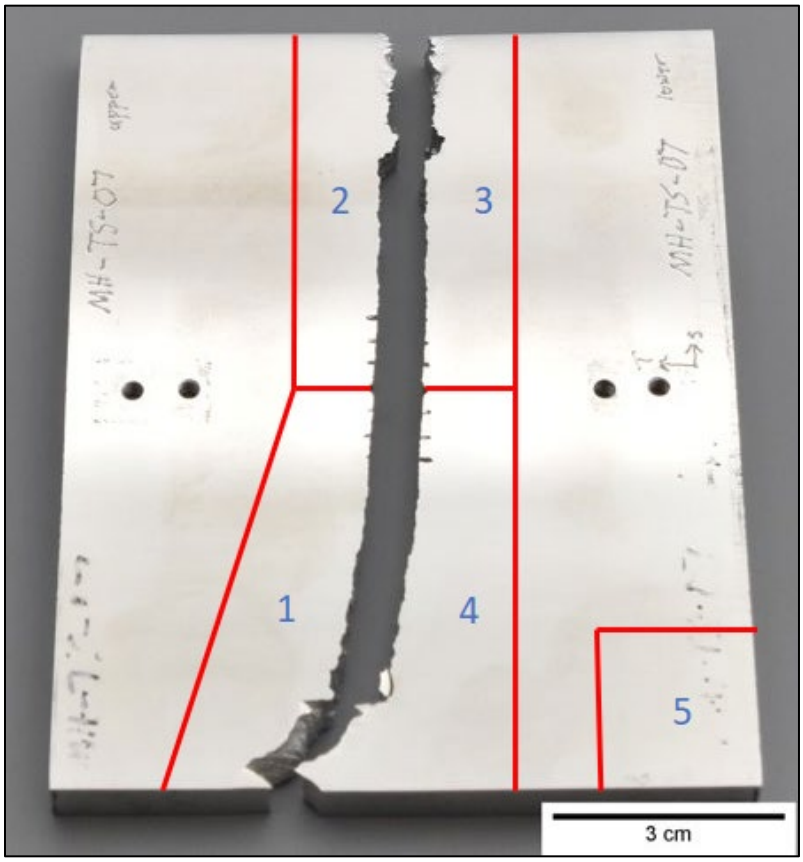

Figure 48.5: Machining instructions for EDM sectioning of center-cracked panel MH-TS-07. Sectioning will result in four fracture edge specimens (numbered 1-4) and one base microstructure specimen (number 5) for each plate.

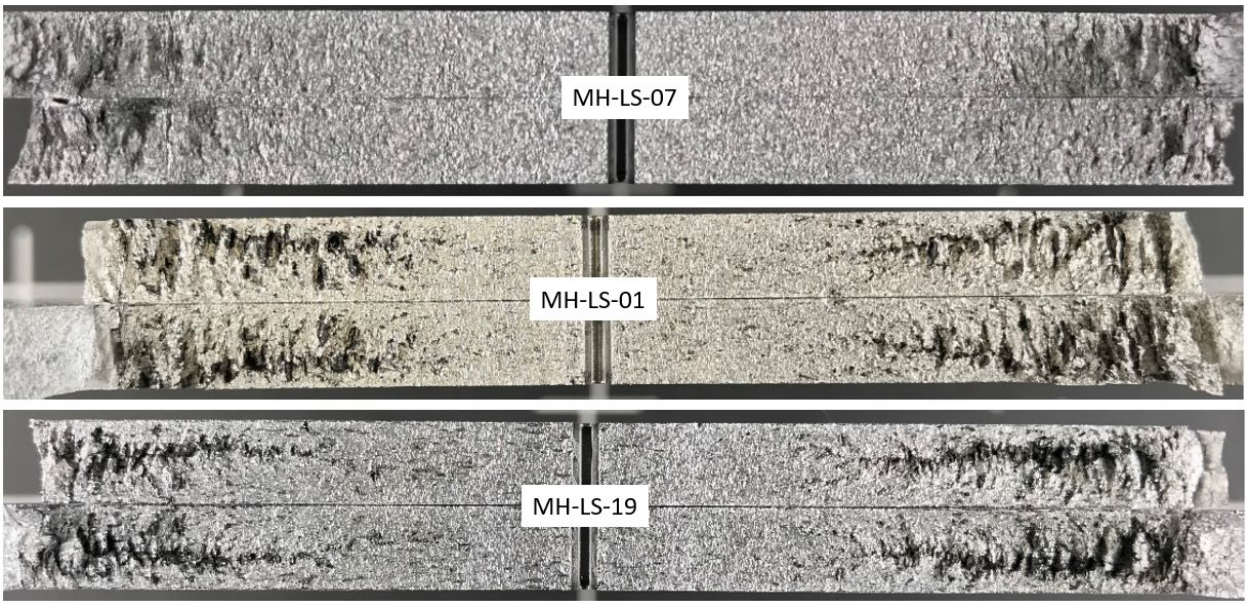

Figure 48.6: Fracture surface images of L-S orientation plates following fatigue testing. Secondary crack networks are observed to have the highest crack density near the centerline thickness for each plate.

Table 48.2: Overview of the preparation procedure for EBSD analysis of Al 7085 fracture specimens.

Step	Description
1	Mounting in epoxy with vacuum impregnation
2	240 grit grinding to establish plane
3	400 grit grinding for damage removal
4	600 grit grinding for damage removal
5	800 grit fine grinding
6	1200 grit fine grinding
7	3 µm and 1 µm diamond polishing
8	0.04 µm colloidal silica polishing
9	0.04 µm colloidal silica vibratory polishing
10	Final cleaning, drying, and preparation for SEM/EBSD

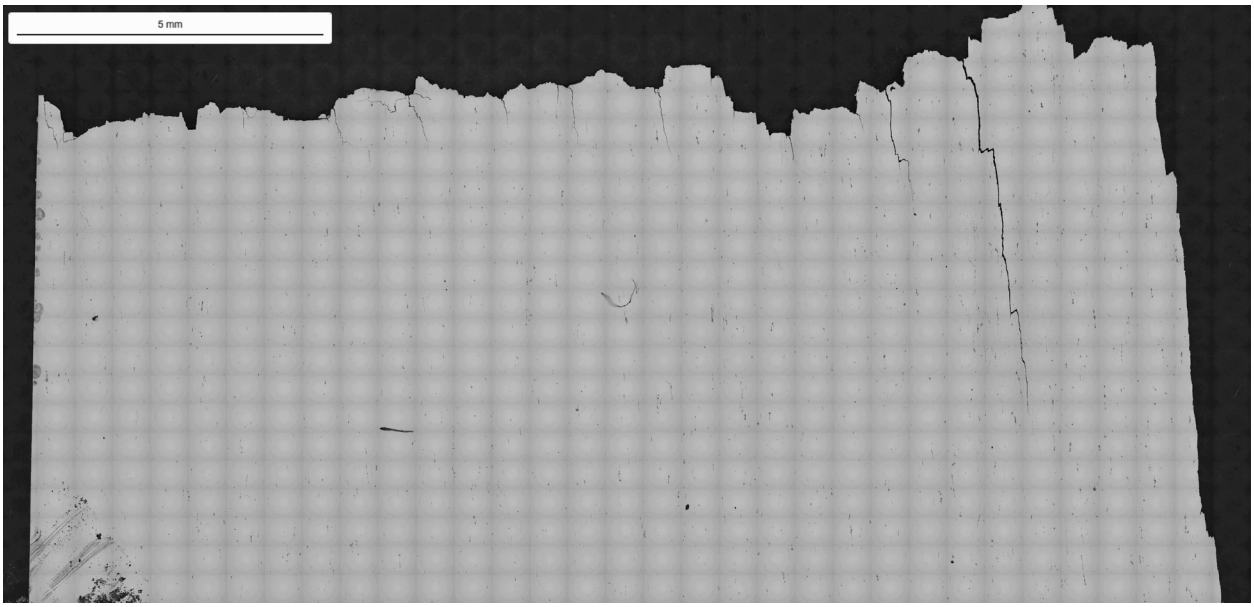

Figure 48.7: Fracture edge optical micrograph mosaic for MH-LS-01, specimen 21A taken at 20X magnification. Large secondary cracks can be seen along the primary fracture edge which progresses horizontally across the top.

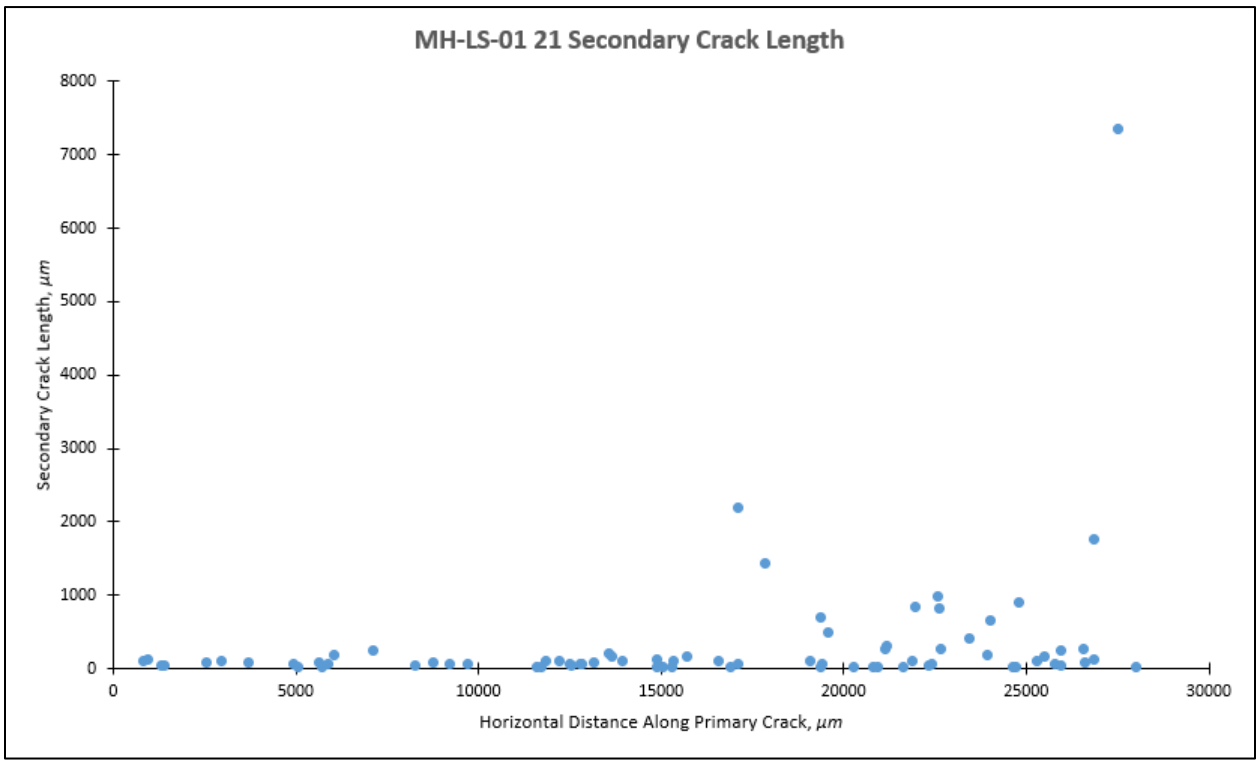

Figure 48.8: Secondary crack lengths along the fracture edge of specimen MH-LS-01, section 21.

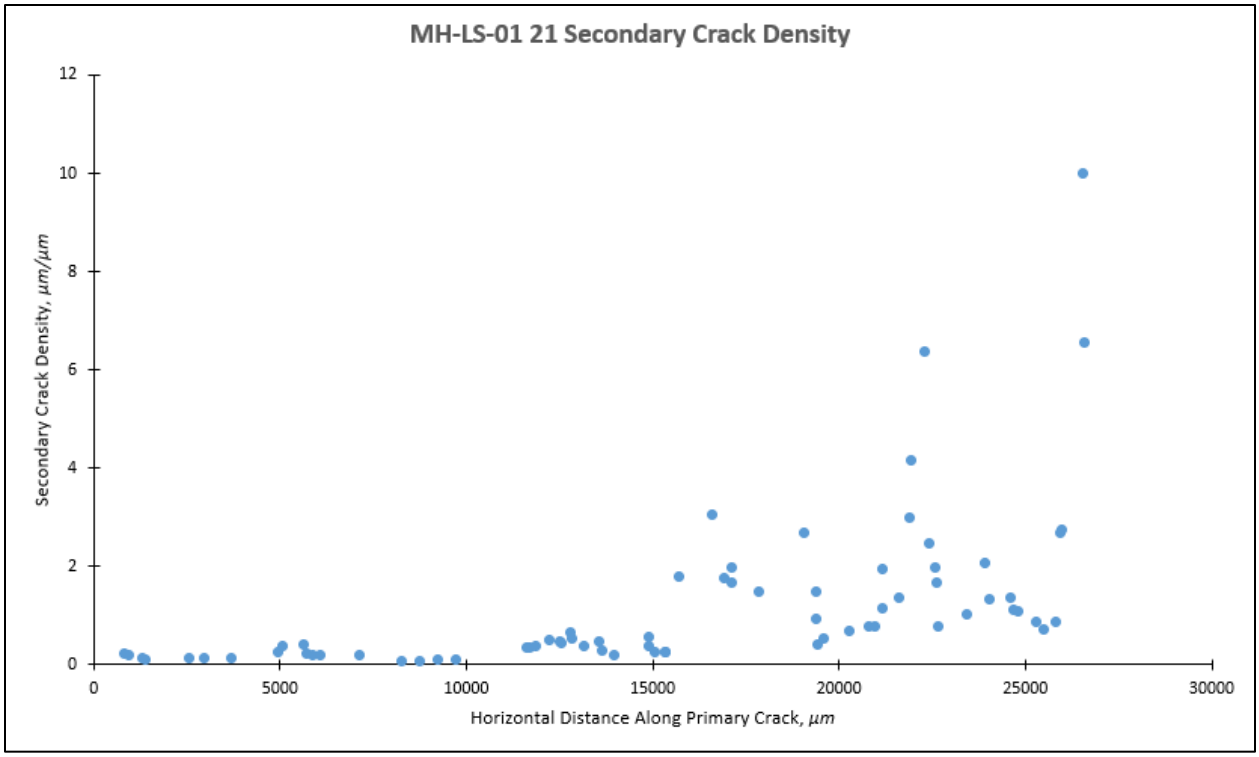

Figure 48.9: Secondary crack density along the fracture edge of specimen MH-LS-01, section 21.

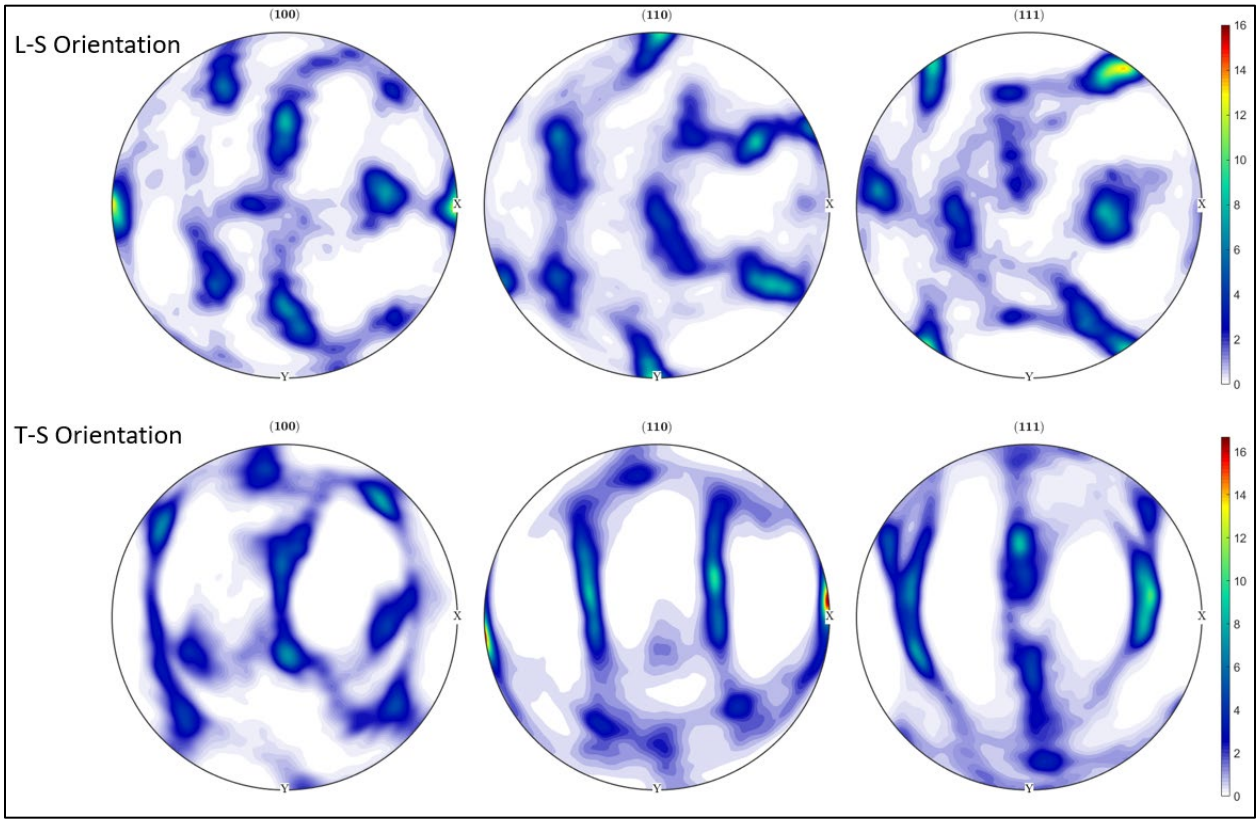

Figure 48.10: Orientation distribution function (ODF) maps for L-S and T-S orientations.

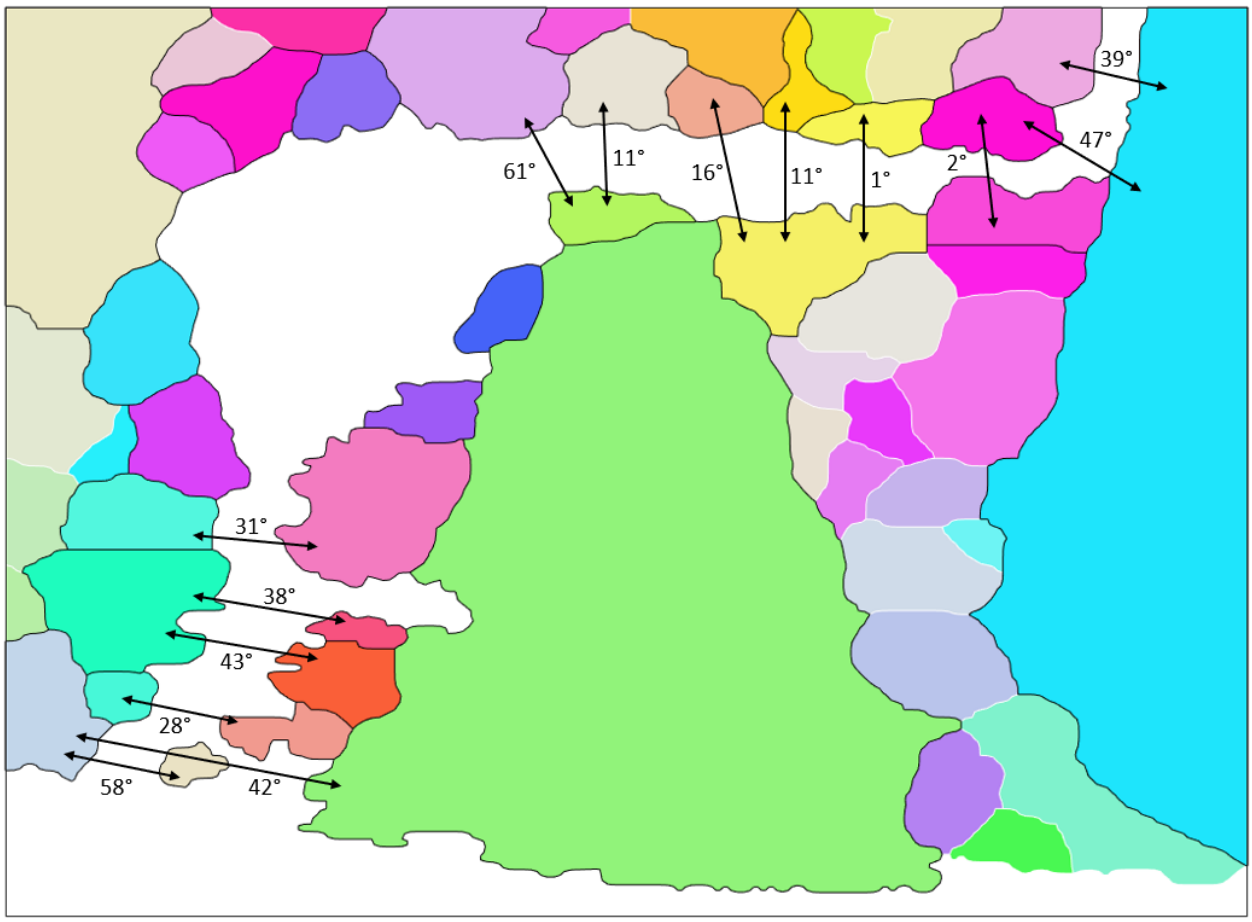

Figure 48.11: Smoothed IPF-Z map of a secondary crack initiation site on MH-LS-01 21A with misorientation angles in degrees overlaid.

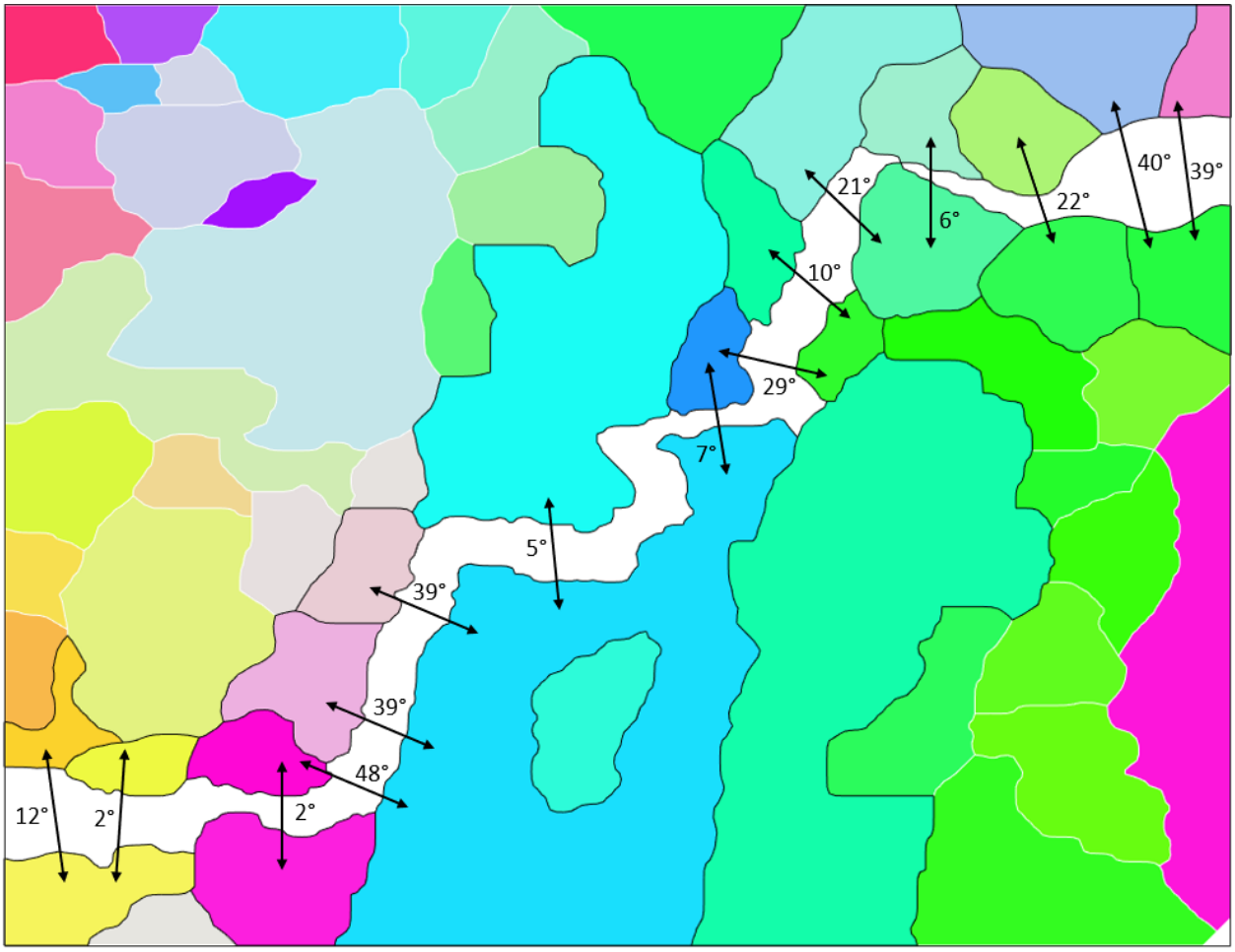

Figure 48.12: Smoothed IPF-Z map of a mixed-direction secondary crack segment on MH-LS-01 21A with misorientation angles overlaid.

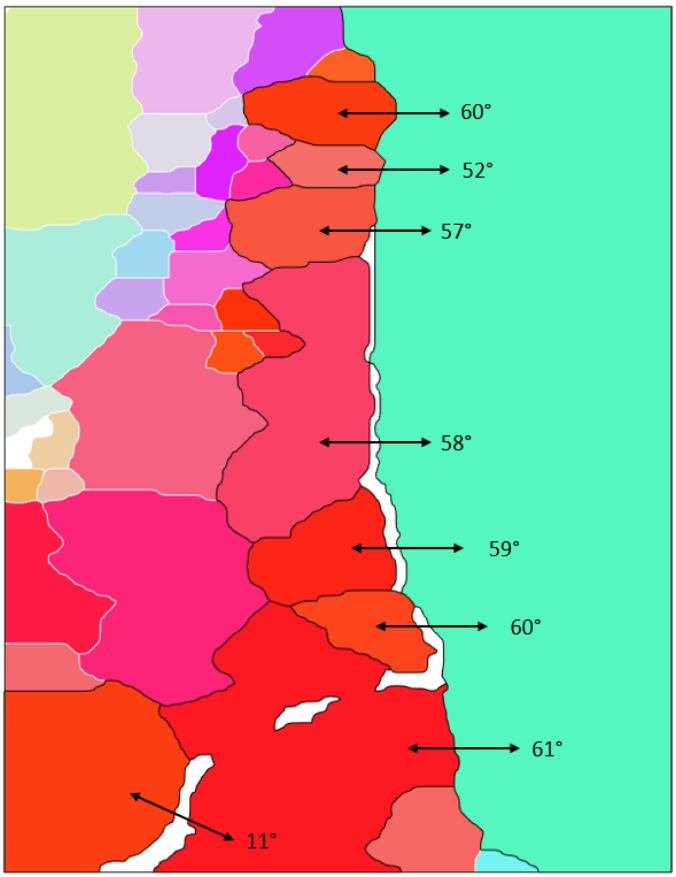

Figure 48.13: Smoothed IPF-Z map of a secondary crack termination site on MH-LS-01 21A with misorientation angles overlaid.

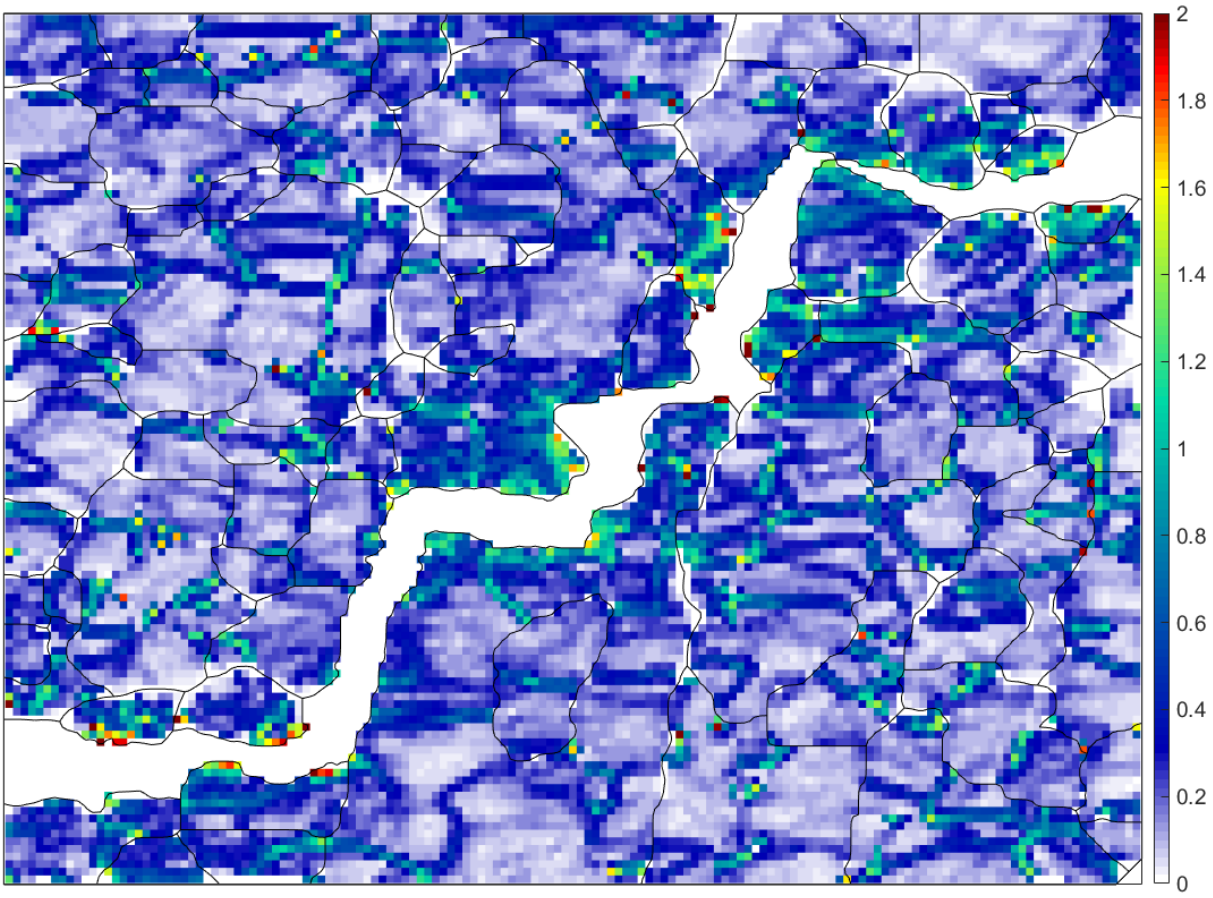

Figure 48.14: Kernel average misorientation (KAM) map of the same area of interest shown in Figure 48.12.